



# Block adjustment and coupled epipolar rectification of LROC NAC images for precision lunar topographic mapping

Han Hu, Bo Wu \*

*Department of Land Surveying and Geo-Information, The Hong Kong Polytechnic University, Hun Hom, Kowloon, Hong Kong*



## ARTICLE INFO

**Keywords:**  
Photogrammetry  
LROC NAC  
Block adjustment  
Epipolar rectification

## ABSTRACT

The narrow-angle camera (NAC) of the lunar reconnaissance orbiter camera (LROC) uses a pair of closely attached pushbroom sensors to obtain a large swath of coverage while providing high-resolution imaging. However, the two image sensors do not share the same lenses and cannot be modelled geometrically with a single physical model. The irregular image network leads to difficulties in conducting the block adjustment to remove inconsistencies between the NAC images in both intra- and inter-track cases. In addition, the special image network requires two to four stereo models, each with an irregular overlapping region of varying size. The stereo configuration of NAC images also creates severe problems for the state-of-the-art image matching methods. With the aim of using NAC stereo pairs for precision 3D topographic mapping, this paper presents a novel approach to the block adjustment and coupled epipolar rectification of NAC stereo images. This approach removes the internal inconsistencies in a single block adjustment and merges the image pair in the disparity space, thus requiring estimation of only one stereo model. Semi-global matching is used to generate a disparity map for the stereo pair; each correspondence is transformed back to the source image, and 3D points are derived via photogrammetric space intersection. The experimental results reveal that the proposed approach is able to reduce the gaps and inconsistencies caused by the inaccurate boresight offsets between the two NAC cameras and the irregular overlapping regions and to finally generate precise and consistent 3D topographic models from the NAC stereo images.

## 1. Introduction

Three-dimensional topographic models of planetary surfaces is essential for planetary exploration and scientific research (Garvin et al., 1999; Robinson et al., 2010; Wu et al., 2013). Although large-scale and even global-scale topographic models can be obtained from laser altimetric data, such as the lunar orbiter laser altimeter (LOLA) (Smith et al., 2010) and the Mars orbiter laser altimeter (MOLA) (Garvin et al., 1999), these datasets generally have a large spatial resolution (e.g., dozens or hundreds of meters). However, operational and research procedures, such as precision landing, maneuvering rovers, astronaut navigation (Wu et al., 2014), and crater morphometry (Watters et al., 2015), require topographic models with meter-level resolution, which can be obtained from high-resolution cameras such as the narrow-angle camera (NAC) on board the lunar reconnaissance orbiter (LRO) (Robinson et al., 2010).

Although the NAC provides unprecedented image resolution for the lunar surface (up to 0.5 m/pixel), the advantages of higher resolution come at the cost of smaller field-of-view (FOV), which is 2.85° using a

700-mm focal length telescope. In this configuration, only 2.5 km swath coverage is provided by the limited sensor size of 5000 pixels. To increase the swath angle, two lenses are bundled together, denoted NAC-L and NAC-R, with NAC-L offset 2.85° from NAC-R, so that the footprints on the lunar surface share the same region in the border of both NACs (Robinson et al., 2010). Furthermore, in addition to having the tilt angle parallel to the sensor direction, the NAC-R is installed slightly forward of the NAC-L in the flight direction. Stereographic NACs are made possible by pointing the satellite at the same region in another orbiter track to form a sufficient convergent angle. In addition, the images are captured at 12 bits and condensed to 8 bits and lossless compressed on-board prior to downlink.

Although the tilt angle between NAC-L and NAC-R is small, the cameras do not share the same lens and thus cannot be modelled with a single rigorous camera model. Furthermore, non-rigid boresight misalignment may occur during the mission operation (Wu and Liu, 2017), even after precise offline ground calibration in a laboratory environment, which further conflicts with a unified camera model. In

\* Corresponding author.

E-mail address: [bo.wu@polyu.edu.hk](mailto:bo.wu@polyu.edu.hk) (B. Wu).

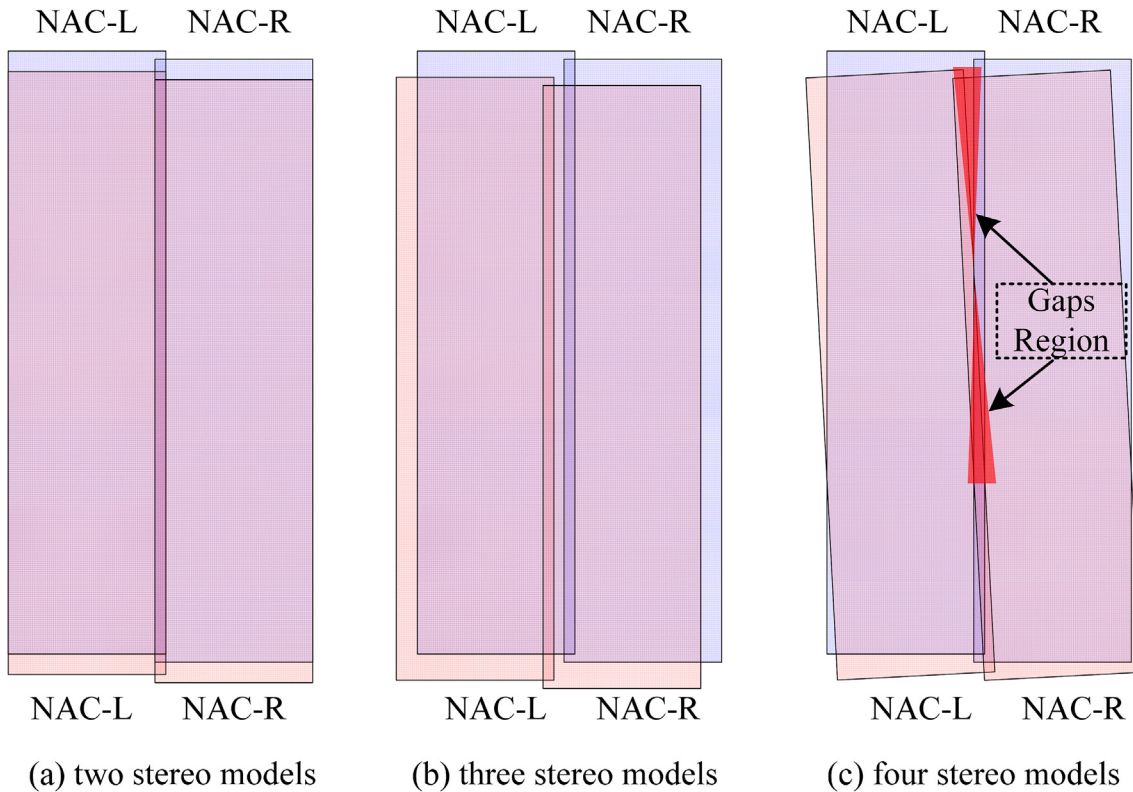


**Fig. 1.** Different theoretical model configurations for a stereo pair of NACs. The last case of four stereo models is the most common. Please note the irregular overlapping region, which may cause gaps because of the insufficient matches obtained.

addition, geometric inconsistencies exist not only between NAC-L and NAC-R in the same orbiter but also between the NAC images from different orbiter tracks. If these inconsistencies are not removed successfully, gaps will appear in the overlapping region between the images.

Another problem with the use of NACs for precision topographic mapping is that for a stereo pair of NACs, four individual images are used to create a digital elevation model (DEM) that covers the entire region, and at least two stereo models are required when the images overlap perfectly, as illustrated in Fig. 1(a). However, in most cases, three or four models need to be formulated, as shown in Fig. 1(b) and (c). It should be noted that in addition to the two major stereo models for NAC-L and NAC-R, one or two more stereo models are required for the NAC-L and NAC-R images from different orbiters. The overlapping area is narrow and irregular, which may impede generation of the DEM, because the most sophisticated dense image matching (DIM) methods require certain initialization steps from a relatively larger context to remove ambiguities in the image matching by geometric constraint (Furukawa and Ponce, 2010; Wu et al., 2012) and improve the robustness by global inference (Hu et al., 2016a,b). Thus, gaps in the overlapping areas may exist due to the failure of DIM in these areas, as depicted in Fig. 1(c).

To resolve this issue, in this paper, we propose a novel approach to block adjustment and coupled epipolar rectification for precision topographic mapping from NAC images. This paper makes two main contributions:

- 1) To remove the geometric inconsistencies, the tie points in the narrow and irregular overlapping region are efficiently handled by separating the feature detection into two parts: (i) the entire image for the regular overlapping region and (ii) the border part for feature matching between NAC-L and NAC-R. In addition, unlike the separated bore-sight calibration and block adjustment (Speyerer et al., 2016; Wu and Liu, 2017), we propose a single combined free-network block

adjustment for all four images, because an abundant number of tie points distributed in both the entire image and the narrow overlap region that connects the four images can be retrieved.

- 2) To remove the irregular overlapping area in the DIM, we observe that although we cannot create a single camera model for the two NACs, because the two sensors are almost parallel, the horizontal disparities are small, if not negligible. Therefore, it is possible to create a seamless mosaic of the images from the two NACs in the epipolar space. After conducting the epipolar rectification of the pairs of stereographic images, we can create a single stereo model between the coupled rectification, which has more regular coverage and is favored by the general DIM algorithms, such as semiglobal matching (SGM) (Hirschmuller, 2008; Hu et al., 2016a). We can then transform the disparity image to the original image space and use different camera models of the NACs for the space intersection.

The remainder of the paper is organized as follows. In the next section, we discuss the related works on DIM and the epipolar rectification of satellite images. Section 3 presents the proposed method for precision topographic mapping using NAC images. In Section 4, we qualitatively and quantitatively evaluate the proposed method using two stereo pairs of NAC images. We provide concluding remarks in the last section.

## 2. Related works

The data for planetary topographic mapping are mainly sourced from two types of sensors: laser altimeters, such as LOLA (Robinson et al., 2010) and MOLA (Smith et al., 2001), and stereo satellite imaging. The first type of sensor measures the range from the spacecraft to the planet surface and is able to directly calculate the point position with the help of the ephemeris and attitude information of the spacecraft. Although the point spacing along the orbiter is quite dense, the distances between the

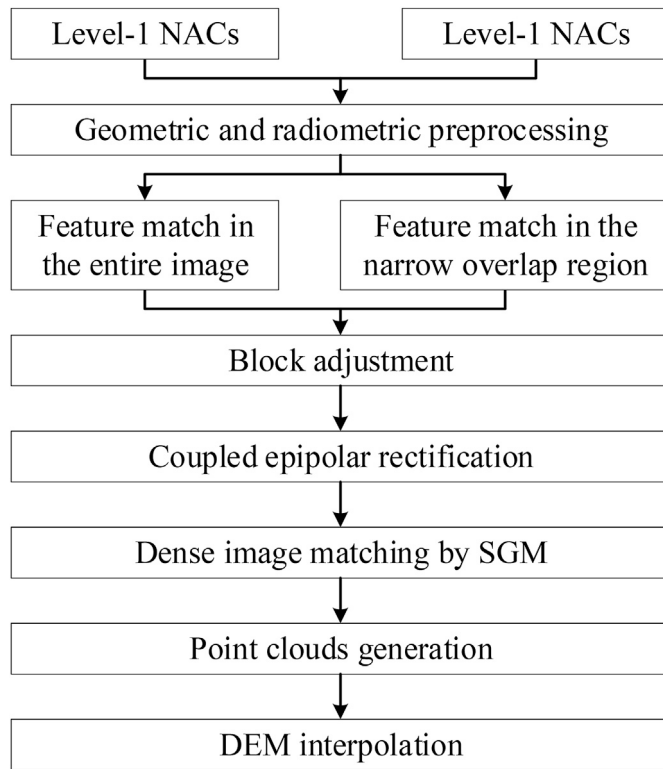


**Fig. 2.** Overall workflow of the approach.

strips are quite large, and the final DEM generated from the laser altimeter suffers from the anisotropic density distribution. However, the points generated from the stereo measurement of satellite images are distributed more evenly and have better spatial resolution (Li et al., 2011; Di et al., 2014; Watters et al., 2015).

The first step in using high-resolution satellite images for precision topographic mapping is to conduct the block adjustment of all the involved images to remove any possible geometric inconsistencies among them. Although this issue has been well-studied for regular image blocks and with certain ground controls or constraints (Di et al., 2014; Wu et al., 2014), the block adjustment of a stereo pair of NACs is still a nontrivial problem due to the irregular geometry of the image network and the absence of ground controls. The literature focuses mainly on the properties of the boresight angle between NAC-L and NAC-R. For example, the temperature-dependent boresight model (Speyerer et al., 2016) improves the orientation parameters of NAC images to generate better precision DEMs. The individually calibrated boresight angle (Wu and Liu, 2017) is difficult to generalize in all cases and needs to be determined for each NAC image pair. Furthermore, the internal inconsistency between the four NAC images can also be reduced in a combined bundle adjustment through automatically detected feature correspondences and the connectivity of the image blocks can be strengthened by manually selected three or four folded tie points, in a commercial photogrammetry system, SOCET SET from BAE Systems (Tran et al., 2010; Mattson et al., 2012; Henriksen et al., 2017). Only a subset of all the exterior orientation parameters are adjusted to avoid correlation of the unknowns and make the optimization better posed. For the external inconsistencies with the reference LOLA DEM, a set of global scaling, translation and rotation parameters is optimized through either profiles of NAC DEM and LOLA points (Henriksen et al., 2017) or sparse points from the bundle adjustment (Moratto et al., 2014). In this paper, we robustly handle the internal inconsistencies by conducting an independent block adjustment for the stereo pairs in a single free network to remove them, with automatically

matched pairwise, three- and four-folded tie points.

After removing the inconsistencies, the next step is to conduct DIM to generate the image correspondences and create a topographic model from the stereo image pairs. Two main DIM strategies, the local and global methods, can be categorized with the use of smoothness constraints and the inference of disparities, respectively (Scharstein and Szeliski, 2002; Hu et al., 2016a). DIM can be interpreted as the procedure for finding a nearest neighbor field of the two-dimensional (2D) base image (Barnes et al., 2009) in the similarity space. To reduce the search complexity, epipolar geometry is generally used to constrain the search to one dimension. Unlike epipolar rectification for a frame camera (Loop and Zhengyou, 1999; Fusiello et al., 2000), the epipolar geometry of pushbroom sensors for most satellite images is a hyperbola rather than a straight line on the stereo pairs (Kim, 2000; Hirschmuller, 2008). Fortunately, because the attitude changes during the collection of a single scene are small, the complicated epipolar geometry can be approximated using some simple functions, such as the affine transformation (Wang et al., 2011; Henriksen et al., 2017), second-order polynomial (Oh et al., 2010), or homographic transformation (de Franchis et al., 2014). After completing the approximate epipolar rectification, the vertical disparities can be removed.

In addition to the epipolar constraints, spatial constraints or the global smooth prior on a large context are commonly used in most DIM algorithms. These constraints or priors are used to remove the ambiguities of image matching in a small local window, which may be caused by repeated textures or textureless areas (Scharstein and Szeliski, 2002; Hu et al., 2016a). For the local methods, Delaunay triangulation is used to assist the propagation and searching of nearby matches (Furukawa and Ponce, 2010; Wu et al., 2012). Expanding the randomly sampled best match to nearby areas also requires a larger overlapped region (Barnes et al., 2009). Furthermore, the global methods generally formulate the image matching as a discrete optimization problem, which can be formulated as a Markov random field (Kolmogorov and Zabih, 2001) or dynamic programming (Scharstein and Szeliski, 2002) and can explicitly impose smooth constraints on the optimization in a larger context.

Due to the abovementioned irregular overlapping of NACs, the performance of the DIM methods generally degrades or even fails when three or four stereo models are generated for one NAC stereo pair (Tran et al., 2010). This problem is especially severe for SGM (Hu et al., 2016a), which aggregates the matching cues in the overall scan lines and adopts the contour information. However, the problem is effectively handled by the coupled epipolar rectification method, which not only reduces the matching problem to only one stereo model, but also removes the problem of the irregular overlap region and reduces the possible gaps in the final matches.

### 3. Precision 3D topographic mapping from LROC NAC images

#### 3.1. Overview of the approach

The overall workflow of the approach includes preprocessing of the NAC images and block adjustment to fix the systematic errors in the exterior orientation parameters between the intra-orbiter and inter-orbiter NACs, coupled epipolar rectification, and DIM for the DEM generation. An overview of the approach is shown in Fig. 2. The input of the approach is a stereo pair of NACs (four images), which are processed to level-1 CDR (calibrated data records) products from the original EDR (experiment data record) (ASU, 2010) using ISIS3 software (USGS, 2017). This process removes the noise in the NAC images and enriches the images with the EO parameters extracted from the SPICE kernel.

For geometric preprocessing, because the NAC-L and NAC-R have different camera frame coordinate systems (Robinson et al., 2010), in particular, the image sampling direction is inverted, the rotation matrix

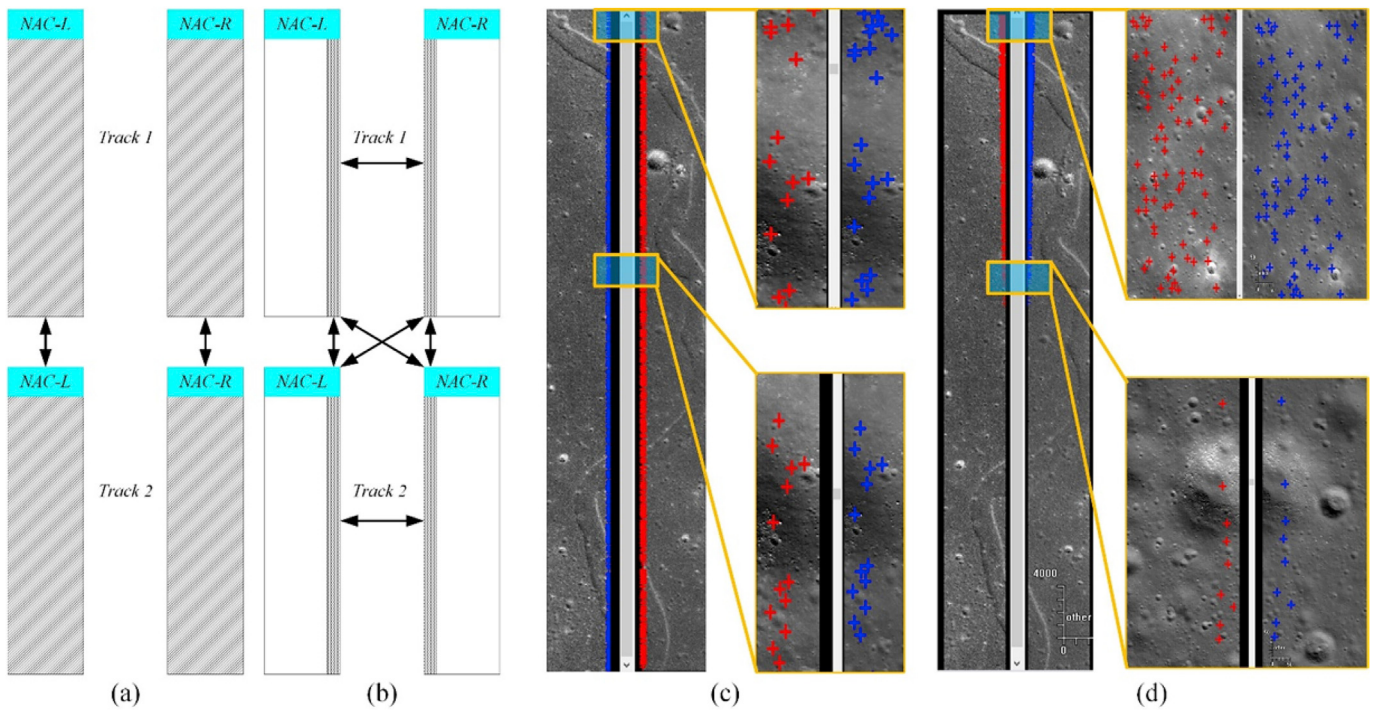


**Fig. 3.** Separated feature matching strategy for block adjustment. Only the shaded areas in the image are used for matching for each set. (a) The first set of feature matches detected on the whole image, where the arrows indicate the pairs for searching the correspondences. (b) The second set of feature matches detected on the overlapping region of NAC-L and NAC-R. (c) Rectangular regions of the feature matches for NAC-L and NAC-R on the same orbiter. (d) Trapezoid regions of the feature matches for NAC-L and NAC-R between different orbiters.

is converted to the same standard system by multiplying an auxiliary rotation matrix  $\mathbf{O}$ , as denoted in the following equation,

$$\mathbf{x} = f\Pi(\mathbf{O}\mathbf{R}(\mathbf{X}-\mathbf{C}))+\mathbf{x}_0 \quad (1)$$

where  $\mathbf{x}$  is the image measurement,  $f$  is the focal length,  $\Pi: \mathbb{R}^3 \rightarrow \mathbb{R}^2$  is the projection function from 3D to 2D,  $\mathbf{R}$  is the rotation matrix obtained in the Level-1 NAC,  $\mathbf{X}$  is the object point position in the geocentric frame,  $\mathbf{C}$  is the translated part of the EO parameter, and  $\mathbf{x}_0$  is the principal point. The different definitions of  $\mathbf{O}$  for NAC-L and NAC-R are as follows,

$$\mathbf{O}_L = \mathbf{R}_z(\pi/2), \mathbf{O}_R = \mathbf{R}_x(\pi)\mathbf{R}_z(\pi/2) \quad (2)$$

where  $\mathbf{R}_x$  and  $\mathbf{R}_z$  denote the rotation matrix around the  $x$  and  $z$  axis, respectively, for a specific angle. The 78 rational polynomial coefficients (RPC) (Grodechi and Dial, 2003) are then fitted for fast projection and consistent description of the different camera models in the block adjustment, using both the intrinsic parameters of the NAC instruments (Robinson et al., 2010) and the extracted EO parameters for the images. For the radiometrical preprocessing, the contrast of the image is enhanced by clipping a specific percentage of the image histogram (2% is adopted in this paper) to the whole sampling space. This step is crucial for feature point matching, because the Level-1 images generally only span a small percentage of the sampling space and appear to be textureless and grayish.

### 3.2. Block adjustment of NAC stereo pairs

Before conducting the DIM in the disparity space, block adjustment of all of the NAC images is needed to remove the vertical disparity of the image pairs between the NAC-L and NAC-R of the same orbiter and the images from different orbiters. However, as shown in Fig. 1, the overlapping region between NAC-L and NAC-R comprises a very small portion of the image. Thus, if the feature points are detected throughout the whole image, the search space for the correspondences will be quite

narrow and will not retrieve sufficient tie points for successful block adjustment. In addition, for the major part of the overlap region, the tie points need to be distributed evenly on the whole image to attain effective block adjustment. Therefore, in this paper, we separate the feature matches into two segregated parts, as shown in Fig. 3. For the first set, feature points are detected on the whole images from both NAC-L and NAC-R, and only the two major overlap regions, as shown in Fig. 1, are searched for correspondences. For the second set, feature points are only detected in the overlapping region between NAC-L and NAC-R. In the same track, this region is fixed at about 150 pixels (Robinson et al., 2010), although this region varies for different configurations, as shown in Fig. 1. Therefore, the region is determined by the union of the geographic locations of the 150 pixels close to the border by back projection using the RPC parameters.

Fig. 3(c) and (d) show the matching results between NAC-L and NAC-R for the same and different tracks, respectively. It can be seen that the region for the same track is almost a rectangular area with a fixed width, whereas the shape is a trapezoid for different tracks, which indicates the difficult gap region in Fig. 1. The standard scale invariant feature transform (SIFT) is used for the feature detection and matching, and a recent variant of random sample consensus (RANSAC), AC-RANSAC (Moisan et al., 2012), is used to remove outliers. After outlier removal is complete, the features are connected into multiple tie points using connected components methods (Agarwal et al., 2011).

For block adjustment, only the additional affine parameter for the RPC coefficient (Grodechi and Dial, 2003) is adjusted for each NAC image. Because no ground control points are available on the lunar surface, the free network block adjustment approach is used. However, even for free network adjustment, weak ground controls are needed to remove the ambiguity of the solver (Fraser and Ravanbakhsh, 2009). Therefore, the initial values of the affine parameters, which are zero translation and rotation, are also considered as weighted observations for the block adjustment. Specifically, the combined block adjustment is formulated as

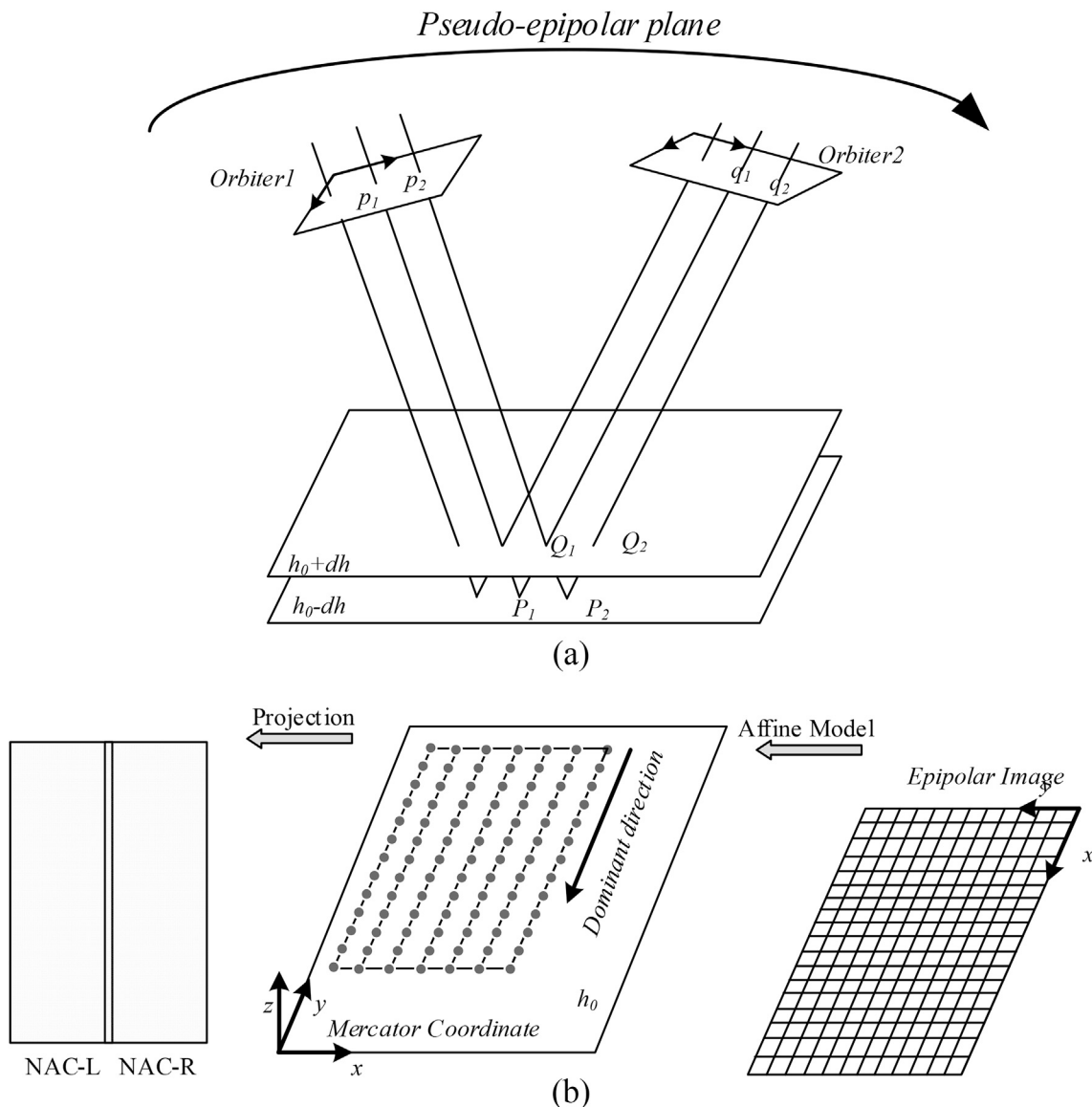


**Fig. 4.** Illustration of the coupled epipolar rectification. (a) Determination of the epipolar curve by iterative projection and back-projection in the pseudo-epipolar plane; and (b) affine resampling of the epipolar image.

follows,

$$\min_{\mathbf{A}, \mathbf{X}} \frac{1}{|Z|} \sum_{i,j} (\mathbf{w}_x^T (\mathbf{A}_i f(\mathbf{X}^j) - \mathbf{x}_i^j))^2 + \frac{\lambda}{|N|} \sum_i \|\mathbf{W}_A \circ (\mathbf{A}_i - \mathbf{A}_0)\|_F^2 \quad (3)$$

where  $\mathbf{A} \in \mathbb{R}^{2 \times 3}$  and  $\mathbf{X} \in \mathbb{R}^3$  are the unknowns for the affine parameters and 3D object points, respectively;  $Z$  and  $N$  are the normalization factors, denoted as the numbers of feature points and images, respectively;  $i$  and  $j$  are the indices of the image and object point, respectively;  $\mathbf{w}_x \in \mathbb{R}^2$  and  $\mathbf{W}_A \in \mathbb{R}^{2 \times 3}$  are the weights for the observations of the tie points and initial affine parameters, respectively;  $f(\cdot)$  is the RPC projection function from the 3D point to 2D image pixel;  $\mathbf{x}$  is the coordinate of the tie points;  $\mathbf{A}_0$  is the initial value of the affine parameters;  $(\circ)$  is the Hadamard product of matrices; and  $\|\cdot\|_F$  is the Frobenius norm of matrix. Equation (3) is a regularized least-squares problem (Hastie et al., 2009), and a standard solver is used for optimization (Agarwal and Mierle, 2010).

### 3.3. Coupled epipolar rectification

As mentioned above, the epipolar geometry for push-broom satellite images is not a straight line. Because the sensor size for the NAC images is relatively small and the attitude variation during the collection in one orbiter is negligible, we have found that the affine model (Wang et al., 2011) is sufficient to describe the epipolar space.

The basic idea is to determine a series of epipolar curves and to align each vertical scanline of the epipolar image parallel to the epipolar curve, as shown in the center of Fig. 4(b). The generation of a single epipolar curve is an analogue of the intersection of the epipolar plane and the image frame for the frame camera, which is denoted as the pseudo-epipolar plane, as shown in Fig. 4(a). We iteratively project and back-project inside the pseudo-epipolar plane to obtain a series of points, as described in Table 1. Although this series of points should be mathematically describable by a hyperbola (Kim, 2000), in practice, it is sufficient to fit the points by a straight line. The direction of this line will help

**Table 1**

Algorithm for tracing an epipolar curve.

*TraceEpipolarCurve*

*Input:* The EO information of a pair of NACs after block adjustment and the center of the forward image as  $p_1$ .

*Output:* A epipolar curve on the forward images  $\{p_i, i = 1, 2, 3 \dots\}$

*Procedure:*

- for  $i = 1, 2, 3, \dots$  until  $p_i$  falls out of the forward NAC
  - 1 Back-project  $p_i$  to the minimum plane as  $P_i$
  - 2 Project  $P_i$  to the corresponding backward NAC as  $q_i$
  - 3 Back-project  $q_i$  to the maximum plane as  $Q_i$
  - 4 Project  $Q_i$  to the corresponding forward NAC as  $p_{i+1}$
- Swap the minimum and maximum plane and repeat the above procedure, this will make the epipolar curve match in the opposite direction

**Table 2**

Information on the experimental NAC stereo pair for the lunar rille area.

Product ID	Resolution (m)	Emission (°)	Incidence (°)
M173246166L	0.52	16.32	49.04
M173246166R	0.52	19.14	49.07
M173252954L	0.51	11.62	48.75
M173252954R	0.50	8.80	48.78

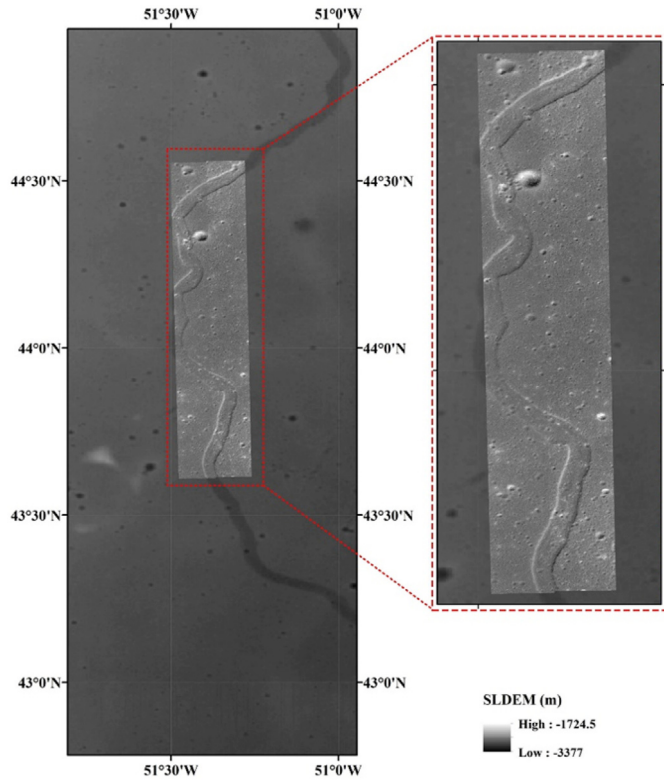


**Fig. 5.** The two NAC images of product M173246166 overlaid on the SLDEM. The images mainly cover part of a long lunar rille. The legend indicates the elevation in meters of the SLDEM in the background.

to determine the dominant direction of the epipolar curve and, unlike the work of Wang et al. (2011), which only involves one curve, we offset the initial point  $p_1$  orthogonal to the curve by a certain distance (512 pixels is used in this paper) and trace a series of curves for both NAC-L and NAC-R. The average direction is then used for the dominant direction.

After tracing each epipolar curve on the NACs, the image points are back-projected to the center plane  $h_0$  of this area in a projected

**Table 3**

Additional affine parameters for the first dataset after the combined block adjustment.

Image	$m_{11}$	$m_{12}$	$m_{13}$	$m_{21}$	$m_{22}$	$m_{23}$
M173246166L	1.0	0.0	0.0	0.0	1.0	0.0
M173246166R	1.0	$-1.9 \times 10^{-6}$	-73.2	$-6.9 \times 10^{-5}$	1.0	27.4
M173252954L	1.0	$3.0 \times 10^{-4}$	118.8	$3.0 \times 10^{-4}$	1.0	-17.7
M173252954R	1.0	$3.0 \times 10^{-4}$	46.5	$-8.6 \times 10^{-5}$	1.0	18.8

coordinate system, and Mercator projection is used for simplicity. The dominant direction is estimated using all of the epipolar curves, and this direction determines the rotation part of the affine transformation between the epipolar image and the projected object space, by which the  $x$  axis of the epipolar image is aligned parallel to the dominant direction. Then, given a ground sample distance of the epipolar image, the scale part of the affine transformation can also be determined. In this way, a one-on-one map between the epipolar image and the object space is established, as shown in the center and right parts of Fig. 4(b).

To obtain the pixel value of the epipolar image, the object point is first projected onto the corresponding NAC-L, and if the image point falls outside of NAC-L, it is then projected onto NAC-R. A mask is also recorded, which indicates the NAC image from which the pixel on the epipolar space is taken. In this way, we are able to use the correct camera model for space intersection.

### 3.4. SGM matching and DEM generation

Following the coupled epipolar rectification, texture-aware SGM (Hu et al., 2016a) is used to generate a disparity image. The SGM algorithm is an extension of dynamic programming, which uses 16 aggregated directions rather than only one direction along the horizontal scanline. In each direction  $r$ , SGM solves the following dynamic programming,

$$\begin{aligned} L_r(p, d) = & C(p, d) + \min(L_r(p - r, d), \\ & L_r(p - r, d - 1) + P_1, \\ & L_r(p - r, d + 1) + P_1, \\ & \min_i L_r(p - r, i) + P_2 - \min_k L_r(p - r, k)) \end{aligned} \quad (4)$$

where  $p$  is the current pixel;  $C(p, d)$  measures the matching cost or dissimilarity at the disparity of  $d$ ; and  $P_1$  and  $P_2$  control the smoothness of the discontinuities of one pixel and more than two pixels, respectively. These two parameters are tuned adaptively according to the image contours, which means that at the object boundaries, the texture aware SGM allows larger fluctuations of the disparities (Hu et al., 2016a).

After applying the SGM, we obtain a disparity map  $d(p)$  of the epipolar image. The disparity map indicates that for each pixel  $p(x, y)$  in the coupled epipolar image from the first orbiter, the correspondence in the epipolar image from the second orbiter is  $p'(x + d(p), y)$ . Furthermore, we can acquire the Boolean values  $b(p)$  and  $b'(p')$  from the accompanying mask for each epipolar image, which describe whether to project onto NAC-L or NAC-R using the transformation indicated in Fig. 4(b). The corresponding EO parameters are then used to triangulate an object point. After processing all of the valid disparities in the epipolar space, the point clouds are interpolated using inverse distance weighting to the gridded DEM.

## 4. Experimental evaluation

Three datasets are used for experimental evaluation. The first is a pair of images with a 0.5-m ground sample distance (GSD) on a long lunar rille area, the second is a pair of images with a 1.2-m GSD on Dorsa Whiston, and the third is a pair of images with a 1.4-m GSD covering part of the Tsinger crater. To evaluate the quality of the epipolar rectification, anaglyphs with cyan-red stereo mode are used to visually validate the removal of the vertical disparity. Furthermore, the coupled epipolar

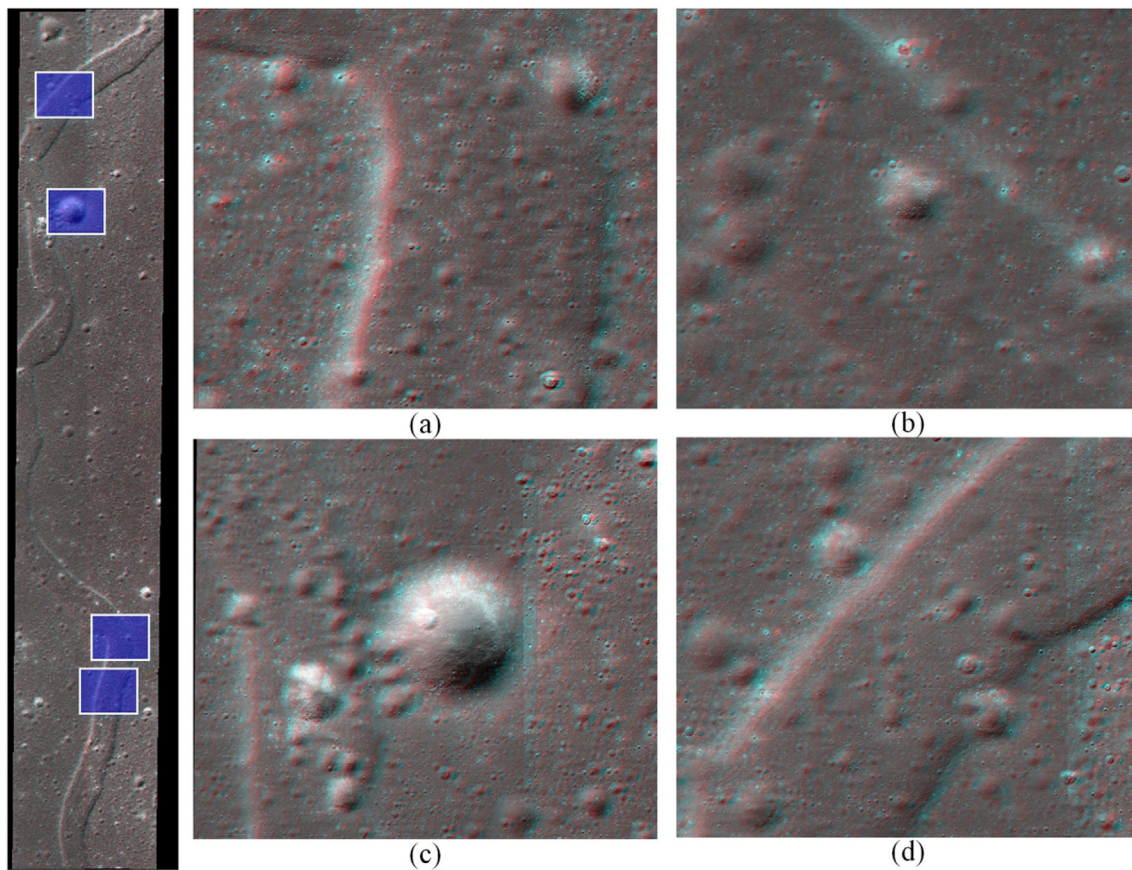


**Fig. 6.** Anaglyphs of the whole epipolar image and selected regions. The enlarged views through (a) to (d) indicate the blue shaded boxes in the left thumbnails from bottom to top. The color bias in the middle of the anaglyphs is caused by the color inconsistency between NAC-L and NAC-R. The color modes of the anaglyphs are red/left to cyan/right. Please wear the appropriate filter glasses to observe the stereo effects. (For interpretation of the references to color in this figure legend, the reader is referred to the Web version of this article.)

**Table 4**

Statistics of the tie points on the epipolar image of the lunar rille area. The first two rows indicate the results for the epipolar images on the same track and the last row for the results of the coupled rectification.

Image Pair	Horizontal (pixels)			Vertical (pixels)			# points
	Min	Max	RMSE	Min	Max	RMSE	
M173246166 (L-R)	-0.68	0.73	0.27	-0.56	0.16	0.27	49
M173252954 (L-R)	-0.69	0.77	0.26	-0.49	0.44	0.19	113
Coupled rectification	N/A			-0.21	0.31	0.09	453

rectification is validated by measuring the vertical and horizontal disparities of the subpixel tie points obtained using the commercial photogrammetric software Leica Photogrammetry Suite (LPS). To evaluate the quality of the mapping results, both the disparity map and DEM are generated and the NAC-DEM is compared with the SLDEM (Barker et al., 2016), which is the most precise DEM publically available for the lunar surface. SLDEM was generated by co-registering  $4.5 \times 10^9$  LOLA heights measurements and 43,200 DEMs from the SELENE Terrain Camera (TC). After co-registration, the root mean square error of vertical residuals between TC DEMs and LOLA DEM is less than 5 m at 90% margin. The SLDEM has a typical vertical accuracy about 3–4 m and a horizontal resolution of 512 pixels per degree (approximately 60 m at the Lunar equator). In addition, for the third dataset, the reference LROC NAC DEM

obtained from the RDR products of LROC (denoted as ASU DEM) is used to validate the DEM quality produced from the proposed method, which is produced from combination of the ISIS and a commercial solution SOCET SET (Henriksen et al., 2017).

#### 4.1. Experiment on NAC images covering a lunar rille area

The first stereo pair of NACs on the long lunar rille is used to evaluate the performance of the proposed method. The details of the stereo pair are listed in Table 2. It should be noted that the convergent angle of the two pairs of NACs is formulated by banking the satellite across the orbit direction and the average convergent angle of the two major overlapping regions is about 19°. In this configuration, the theoretical measurement accuracy at the corresponding altitude is about 1.5 m according to the baseline-height ratio estimation (Cook et al., 1996) at a matching accuracy of 1 pixel for SGM (Scharstein et al., 2017). All the images have the same dimension of 5064 × 52,224 pixels. The overlapping region for NAC-L and NAC-R in the same orbit is a rectangle area with about 150 pixels wide. The overlapping regions for NAC-L and NAC-R from different orbits formulate two triangles with the widest part of about 400 pixels at the top (or bottom) of the images. Fig. 5 overlays the NACs in the first track on top of the SLDEM. The center of the two NACs is around 44°N and 51.5°W. The images cover part of a long lunar rille, which was possibly formed from a lava channel in the early age of the moon. An enlarged view of the georeferenced images is also shown in the right part of Fig. 5.

For the block adjustment, the feature matching and track connection

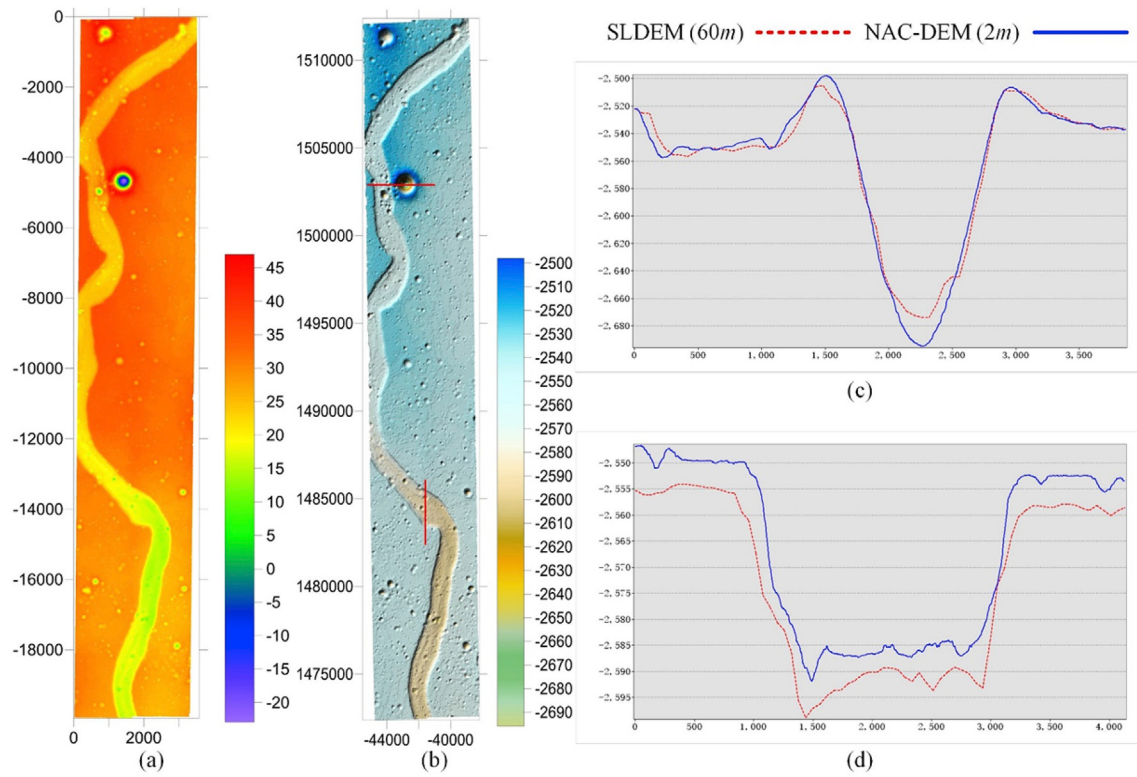


**Fig. 7.** Disparity map and DEM of the stereo pair. (a) Disparity map of the coupled rectification images; (b) shaded relief map of the DEM, the elevation is exaggerated by five times to better reveal the terrain surface and relief shading effect; (c) and (d) the profile comparisons of the horizontal and vertical red lines in (b), respectively, between the SLDEM and NAC-DEM. The metrics in the legend indicate the resolution of the corresponding DEM. (For interpretation of the references to color in this figure legend, the reader is referred to the Web version of this article.)

produce 23,253 object points. In the bundle adjustment, we remove several outliers using the 68–95–99.7 rule of  $3\sigma$ , and 23,043 object points contribute to the final bundle adjustment, with a subpixel level of  $\sigma_0$  at 0.7 pixels. This indicates a successful bundle adjustment. The *a priori* standard deviation used for weight determination of the pixel observations is set to 1 pixel. And for the affine parameters, the six terms are split into rotation and translation parts, for which the standard deviation is set to 0.0001 and 50 pixels, respectively. The weights are the reciprocals of the *a priori* standard deviations. The balance parameter  $\lambda$  for the observations of feature points and affine parameters is fixed as 0.01. The affine parameters after block adjustment for all the images are listed in Table 3. It can be noticed that the inconsistency between NAC-L and NAC-R in the same orbit are all around  $-73$  pixels for both orbits.

In theory, the epipolar rectification removes the vertical disparities in the images. However, it is possible to visually perceive the stereo effect formulated by two epipolar images, as long as each eye only observes a single epipolar image. This not only provides an effective method for direct 3D measurements, but also a quick approach for qualitative evaluation of the epipolar rectification. If the rectification is not satisfactory, large vertical disparities will be apparent in the two epipolar images together with other visually observable noises and the stereo effects will be degraded.

In this paper, we create anaglyphs by overlaying the two grayscale images, with the red channel for the left epipolar image and the green and blue channels for the right epipolar image. This is commonly known as the red-cyan stereo mode. The whole anaglyph is located in the left part of Fig. 6, in which the shaded blue squares indicate enlarged views of four representative areas along the rille. The squares from top to the bottom represent subfigures Fig. 6 (a) through (d), respectively. With the corresponding filters, the anaglyphs can be seen to show strong stereo effects, which indicates that the epipolar rectification is of good quality, with no apparent vertical disparities. The flat parts, which are outside the

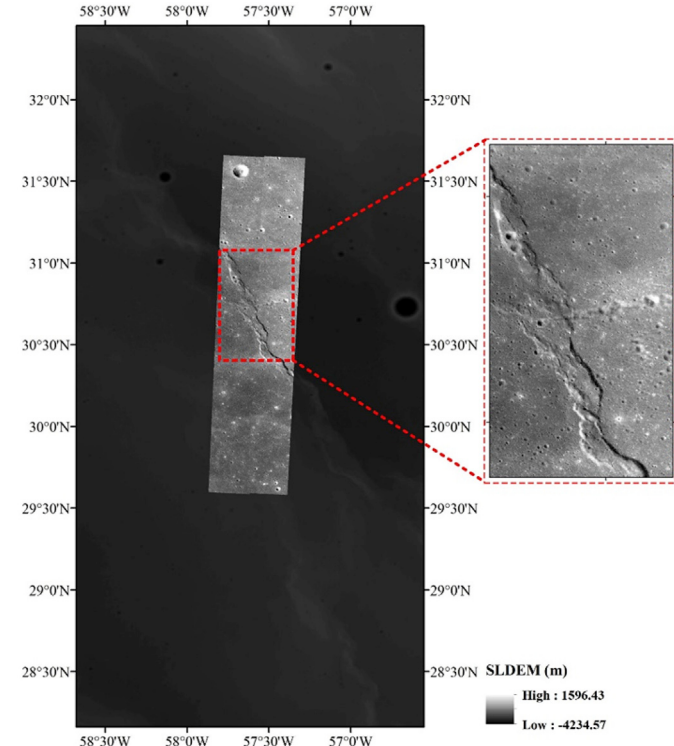


**Fig. 8.** The two NAC images of product M1206392603 overlaid on the SLDEM. The images mainly cover part of the long wrinkle ridge, as shown in the background SLDEM, and a series of continuous craters, as shown on the highlighted right part. The legend indicates the elevation in meters of the SLDEM in the background.

**Table 5**

Information on the experimental NAC stereo pair for Dorsa Whiston.

Product ID	Resolution (m)	Emission (°)	Incidence (°)
M1206392603L	1.24	18.13	45.91
M1206392603R	1.23	15.18	46.08
M1206406672L	1.20	9.03	47.32
M1206406672R	1.21	11.98	47.49

craters or rilles, present relatively small parallax; this is because the epipolar image is rectified in the horizontal plane of the average elevation in the covered area. In addition, the color bias in the middle part of the anaglyphs in Fig. 6 (c) and (d) is caused by the inherent color differences between the NAC-L and NAC-R, as shown in Fig. 5. Although local color balancing may be required prior to the generation of anaglyphs and orthoimages for better visual presentations, this is out of the scope of this paper.

Furthermore, a basic assumption of coupled epipolar rectification is that the horizontal disparity between the epipolar images of NAC-L and NAC-R should be small if not zero. This assumption can be visually validated in the anaglyphs in Fig. 6 because, except for the intensity difference, there are no obvious geometric inconsistencies between NAC-L and NAC-R. In addition, the horizontal disparity and vertical disparity are validated by the subpixel tie points matching using LPS. The statistics of the matching results are recorded in Table 4. It should be noted that for the epipolar images of NAC-L and NAC-R in the same track, the horizontal disparity does not exceed 1 pixel and the root mean squared error

(RMSE) is less than 0.3 pixels, which validates the assumption of coupled epipolar rectification. As expected, the RMSE for the vertical disparity is almost 0.1 pixels for the coupled rectification, which indicates that a bottleneck lies in the subpixel capabilities of least-squares matching (Hu et al., 2016b).

For the topographic mapping, the sampling distance for the NAC DEM is set to 2-m, which is a commonly used DEM sampling strategy at three to five times the original image resolution. The matching results are shown in Fig. 7, in which the disparity maps of the coupled epipolar images for the NACs of the first orbiter are shown in Fig. 7 (a) and the shaded relief map of the DEM is shown in Fig. 7 (b). In addition, two profile comparisons between SLDEM and NAC-DEM are shown in Fig. 7 (c) and (d). It should be noted that the NAC-DEM has more detailed information than the SLDEM and that the crater is obviously deeper than that of the SLDEM, probably because the SLDEM has few points sampled in the crater and the DEM is excessively interpolated, and thus the depth is shallower. Furthermore, we notice a slight shift, about 200 m in the horizontal direction, between the SLDEM and NAC-DEM, which is due to the systematic errors in the EO parameters of the NAC images. This phenomenon was also observed in a previous study (Tran et al., 2010). The shift was compensated using a translational model through several tie points interactively identified on the two DEMs.

#### 4.2. Experiment on NAC images of the Dorsa Whiston

The second NAC dataset used in this paper depicts a region of the

**Table 6**

Additional affine parameters for the second dataset after the combined block adjustment.

Image	$m_{11}$	$m_{12}$	$m_{13}$	$m_{21}$	$m_{22}$	$m_{23}$
M1206392603L	1.0	0.0	0.0	0.0	1.0	0.0
M1206392603R	1.0	$-3.4 \times 10^{-6}$	-95.4	$1.4 \times 10^{-4}$	1.0	3.8
M1206406672L	1.0	$1.3 \times 10^{-5}$	30.8	$3.0 \times 10^{-4}$	1.0	$-2.8 \times 10^{-3}$
M1206406672R	1.0	$1.7 \times 10^{-5}$	-66.1	$9.9 \times 10^{-6}$	1.0	-1.9

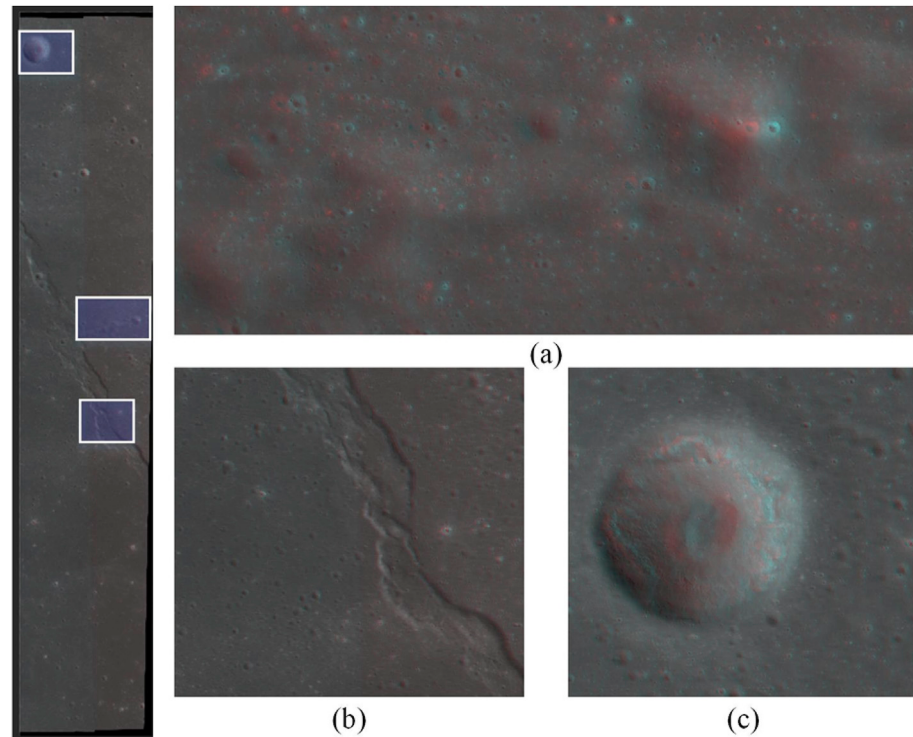


**Fig. 9.** Anaglyphs of the whole epipolar image and selected regions. The enlarged views in (a) through (c) indicate the blue shaded boxes in the left thumbnails. The color modes of the anaglyphs are red/left to cyan/right. Please wear the appropriate filter glasses to observe the stereo effects. (For interpretation of the references to color in this figure legend, the reader is referred to the Web version of this article.)

**Table 7**

Statistics of the tie points on the epipolar image for Dorsa Whiston. The first two rows show the results for the epipolar image of the same track, and the last row shows the results of the coupled rectification.

Image Pair	Horizontal (pixels)			Vertical (pixels)			# points
	Min	Max	RMSE	Min	Max	RMSE	
M1206392603 (L-R)	-0.47	0.23	0.10	-0.15	0.22	0.06	70
M1206406672 (L-R)	-0.43	0.15	0.09	-0.50	0.08	0.31	60
Coupled Rectification	N/A			-0.70	0.38	0.26	254

Dorsa Whiston, which is a wrinkle ridge system in the Oceanus Procellarum on the Moon, as shown in the SLDEM and NAC images in the left part of Fig. 8. Wrinkle ridges, which are a common feature on lunar maria, are assumed to have been created when the basaltic lava cooled and contracted. In addition to the wrinkle ridge system, the stereo image pair features a series of continuous craters, as shown in the subset of the NAC images in the right part of Fig. 8. The information of the NAC images of the two tracks are summarized in Table 5. It should be noted that the resolutions of the two images are around 1.2 m and the convergent angle of the two orbits is about 12°. With this configuration, the theoretical measurement accuracy in the vertical direction is about 6 m. All the images have the same dimension of 5064 × 52,224 as the previous dataset. Although the convergent angle of this dataset is slightly different from the previous dataset, the overlapping region in the same orbit and between two orbits are quite similar.

The block adjustment of the four images begins with 30,222 object points. After 10 iterations of adjustments and outlier removal, the optimization results in 29,284 valid object points with a standard deviation of unit weight of  $\sigma_0=0.8$  pixels, which is good enough, considering that the block adjustment is also regularized by the initial affine parameters. The weights and the parameter  $\lambda$  are the same as the first dataset. And the affine parameters after the combined block adjustment are listed in

**Table 6.** The offsets in the sample direction for each orbit are quite similar.

The cyan/red anaglyphs shown in Fig. 9 are used to validate the coupled epipolar rectification for the Dorsa Whiston. It should be noted that the small craters in Fig. 9(a) align horizontally quite well, which indicates that the combined block adjustment has successfully removed the vertical disparity of the images and that the coupled rectification model is capable of successful approximation of the complex epipolar geometry of the NAC images. Furthermore, the major crater in the top left of the selected region, as shown in Fig. 9(c), has a more abrupt slope and greater depth than the other craters, as shown in Fig. 9(a). To quantitatively analyze the quality of the coupled epipolar images, dozens of tie points are extracted separately in the LPS, and the statistics of the horizontal and vertical disparities are reported in Table 7. The RMSE of the horizontal disparity is around 0.1 pixels and even the maximum value does not exceed 1 pixel. Similar results are also found for the vertical disparity and the case of coupled rectification.

To evaluate the topographic mapping results, the GSDs of both the epipolar image and the DEM are set at 4 m on the Mercator coordinate system, as shown in Fig. 4, which is about three times the GSD of the NAC images. The profile comparison of the two adjacent craters on the wrinkle edge in Fig. 10(c) clearly reveals the details of the DEM and shows that

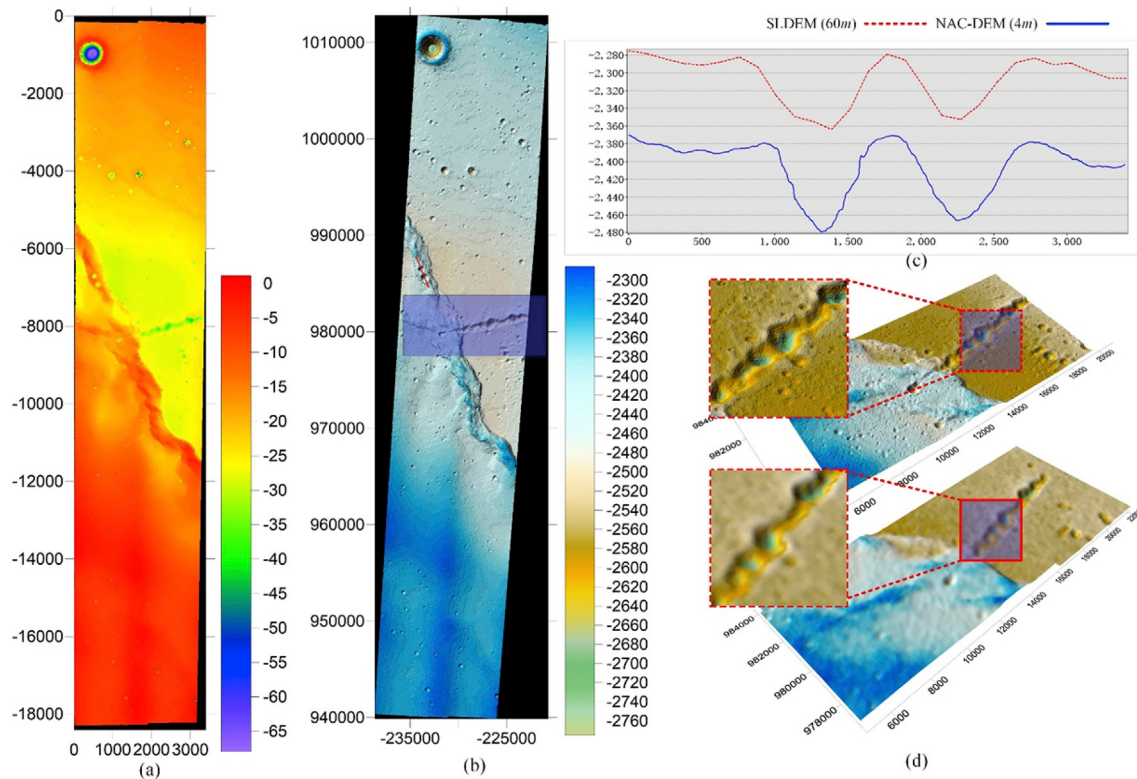


**Fig. 10.** Disparity map and DEM of the stereo pair for Dorsa Whiston. (a) Disparity map of the coupled rectification images; (b) shaded relief map of the DEM (elevation is exaggerated by five times to better reveal the terrain surface and relief shading effect); (c) profile comparison of the red line in (b); and (d) enlarged views of the 3D surface for NAC-DEM (top) and SLDEM (bottom). The metrics in the legend indicate the resolution of the corresponding DEM. (For interpretation of the references to color in this figure legend, the reader is referred to the Web version of this article.)

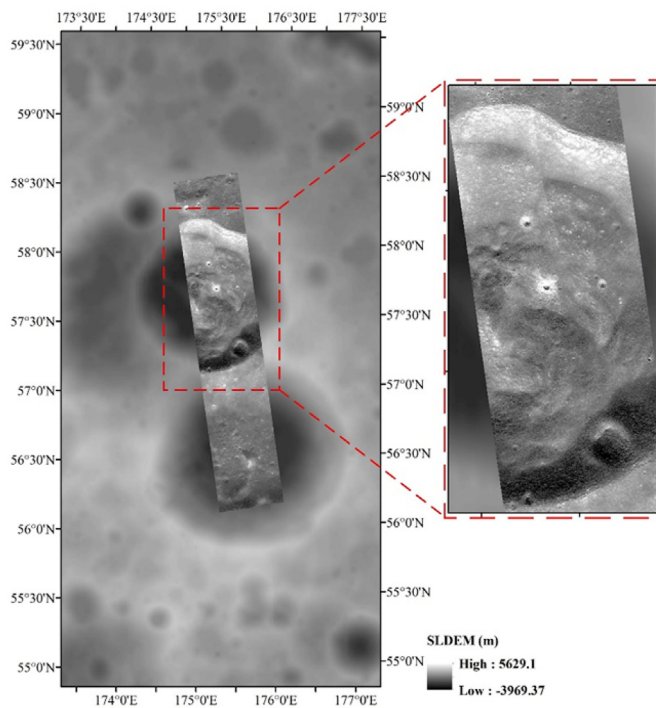


**Fig. 11.** The two NAC images of product M1224828235 overlaid on the SLDEM. The images cover part of the Tsinger crater. The legend indicates the elevation in meters of the SLDEM in the background.

**Table 8**  
Information on the experimental NAC stereo pair for the Tsinger crater.

Product ID	Resolution (m)	Emission (°)	Incidence (°)
M1224828235L	1.42	9.83	58.45
M1224828235R	1.43	12.81	58.45
M1224849339L	1.42	12.86	58.27
M1224849339R	1.41	9.88	58.27

the SLDEM presents the distinct effects of the linear interpolation caused by insufficient points. The NAC-DEM preserves much better terrain details. The shift in the horizontal direction is about 1 km and is compensated through interactive georeferencing between the two DEMs. In addition, a noticeable vertical discrepancy of about 100 m is also presented in Fig. 10(c). This problem is caused by the initial EO parameters of the NAC images, because only free network block adjustment is used. Similar differences in the terrain details can also be observed in Fig. 10(d), in which the terrain features in the SLDEM are smoothed and some small craters are even omitted.

#### 4.3. Experiment on NAC images of Tsinger crater

The third NAC dataset used in this paper depicts a region of the Tsinger crater, which is located in the northern part of the far side of the Moon, as shown in Fig. 11. It can be noted that, although there are some subsequent impacts nearby, the Tsinger crater has escaped from the significant erosion from the subsequent impacts and the rim edge of the

crater still remains relatively sharp as shown in the right part of Fig. 11. The information of the NAC images of the two tracks are summarized in Table 8. The convergence angle of the two orbits is about 18°. At the corresponding spacecraft altitude of 140 km, the theoretical vertical accuracy is about 4.5 m. All the images have the same dimension of 5064 × 52,224 pixels as the previous datasets. Because the latitude of this dataset, at about 60°N, is higher than the previous datasets, the ground paths of the two orbits are slightly crossed, which leads to a relatively small coverage on the bottom part of the stereo pair.

However, the slightly decrease of overlapping area will not influence the final output and the proposed method is still capable of retrieving enough multiple folds of tie points for the block adjustment. The block adjustment of the four images begins with 33,315 object points. After several iterations of adjustment and outlier removal, the optimization results in 32,559 valid object points with a standard deviation of unit weight of  $\sigma_0=0.54$  pixels. The weights and the parameter  $\lambda$  are the same as the previous datasets. And the affine parameters after the combined block adjustment are listed in Table 9. The offsets in the sample direction for the two orbiters are all around 100 pixels.

For the topographic mapping, the sampling distance for the NAC DEM is set to 5 m, which is the same as the ASU-DEM obtained from the LROC data archives. The results are shown in Fig. 12, in which the disparity map and the shaded relief map of the DEM are displayed in Fig. 12(a) and (b), respectively. Because the ASU DEM is co-registered with the reference SLDEM using profile optimizations (Henriksen et al., 2017) and the proposed method only adopts the free network block adjustment, several hundreds meters of discrepancies in both horizontal and vertical directions are observed. Before profile comparison as shown in Fig. 12 (c) and (d), a translational model is used to register the two DEMs in the horizontal direction. Although, in the profiles, the two profiles show a constant height difference, both DEMs are quite consistent, even for some small features, which has indicated that the quality of the DEM from the proposed method is on par with the reference ASU-DEM produced from a commercial solution. Furthermore, as indicated by Henriksen et al. (2017), the generation of the ASU-DEM involves a lot interactions in selecting tie points for bundle adjustment and outlier removing in DEM production, while the proposed method is a fully automatic procedure.

#### 5. Conclusions

In this paper, we introduce a novel approach for the block adjustment and coupled epipolar rectification for lunar topographic mapping from LROC NAC images. The block adjustment effectively removes the internal inconsistencies in the NAC images. Furthermore, the proposed method resamples the NAC-L and NAC-R images from the same platform with two different lenses bundled into the same epipolar image. In this way, the number of stereo models required to reconstruct the whole overlapped area is reduced from three or four to only one. The basic assumption that only a negligible horizontal disparity exists between the epipolar images of NAC-L and NAC-R is confirmed by the tie points in the overlapped area. As evidenced by the anaglyphs and DEMs in the experimental analysis, no inconsistencies or noises are visually noticeable in the overlapping area between NAC-L and NAC-R, which demonstrates that the block adjustment and coupled epipolar rectification model are tenable. Comparison of the SLDEM and NAC-DEM reveals that the details of the latter significantly exceed those of the former.

The approach presented in this paper can facilitate high-resolution

**Table 9**  
Additional affine parameters for the third dataset after the combined block adjustment.

Image	$m_{11}$	$m_{12}$	$m_{13}$	$m_{21}$	$m_{22}$	$m_{23}$
M1224828235L	1.0	0.0	0.0	0.0	1.0	0.0
M1224828235R	1.0	$7.6 \times 10^{-6}$	-99.3	$9.9 \times 10^{-5}$	1.0	3.39
M1224849339L	1.0	$-3.7 \times 10^{-5}$	-106.1	$-2.8 \times 10^{-4}$	1.0	-4.7
M1224849339R	1.0	$-3.8 \times 10^{-5}$	-204.3	$-2.3 \times 10^{-4}$	1.0	-4.4

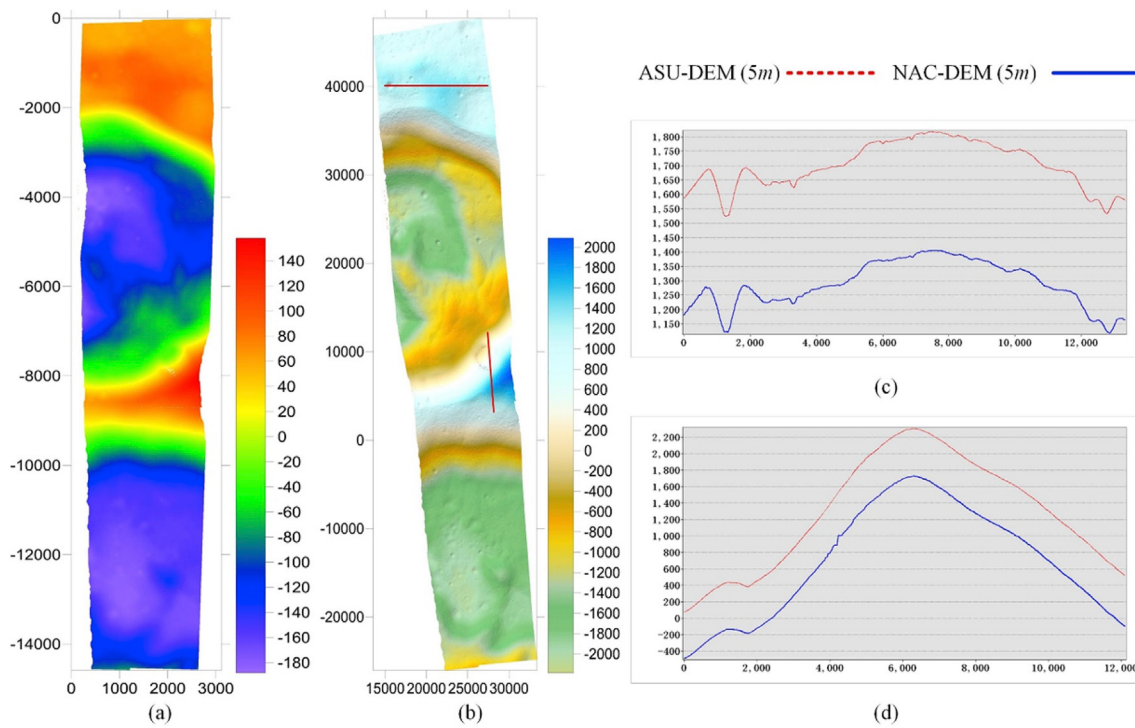


**Fig. 12.** Disparity map and DEM of the stereo pair at Tsinger crater. (a) Disparity map of the coupled rectification images; (b) shaded relief map of the DEM; (c) and (d) the profile comparisons of the horizontal and vertical red lines in (b), respectively, between the ASU-DEM and NAC-DEM obtained from the proposed method. The metrics in the legend indicate the resolution of the corresponding DEM. (For interpretation of the references to color in this figure legend, the reader is referred to the Web version of this article.)

LROC NAC images to be used for high-precision and high-quality 3D topographic mapping of the lunar surface. The approach can also be used in a variety of applications, such as landing site mapping and selection, rover maneuvering, and geological analyses of the lunar surface that require high-quality topographic data.

## Acknowledgments

The work described in this paper was funded by a grant from the Research Grants Council of Hong Kong (Project No.: PolyU 152086/15E) and grants from the National Natural Science Foundation of China (Project No.: 41471345 and Project No.: 41671426).

## References

- Agarwal, S., Furukawa, Y., Snavely, N., Simon, I., Curless, B., Seitz, S.M., Szeliski, R., 2011. Building rome in a day. *Commun. ACM* 54 (10), 105–112.
- Agarwal, S., Mierle, K., 2010. Ceres Solver. <http://ceres-solver.org/> (Accessed August 30th, 2016).
- ASU, 2010. LROC EDR/CDR Data Product Software Interface Specification. [http://lroc.sese.asu.edu/data/LRO-L-RLOC-2-EDR-V1.0/LROLRC\\_0001/DOCUMENT/LROCSIS.PDF](http://lroc.sese.asu.edu/data/LRO-L-RLOC-2-EDR-V1.0/LROLRC_0001/DOCUMENT/LROCSIS.PDF) (Accessed 3rd June, 2017).
- Barker, M.K., Mazarico, E., Neumann, G.A., Zuber, M.T., Haruyama, J., Smith, D.E., 2016. A new lunar digital elevation model from the lunar orbiter laser altimeter and SELENE terrain camera. *Icarus* 273, 346–355.
- Barnes, C., Shechtman, E., Finkelstein, A., Goldman, D., 2009. PatchMatch: a randomized correspondence algorithm for structural image editing. *ACM Trans. Graph.-TOG* 28 (3), 24.
- Cook, A.C., Oberst, J., Roatsch, T., Jaumann, R., Acton, C., 1996. Clementine imagery: selenographic coverage for cartographic and scientific use. *Planet. Space Sci.* 44 (10), 1135–1148.
- de Franchis, C., Meinhardt-Holzapfel, E., Michel, J., Morel, J., Facciolo, G., 2014. On stereorectification of pushbroom images. In: Proc. Image Processing (ICIP), 2014 IEEE International Conference on. IEEE, pp. 5447–5451.
- Di, K., Liu, Y., Liu, B., Peng, M., Hu, W., 2014. A self-calibration bundle adjustment method for photogrammetric processing of Chang'E-2 stereo lunar imagery. *IEEE Trans. Geosci. Rem. Sens.* 52 (9), 5432–5442.
- Fraser, C., Ravabakhsh, M., 2009. Georeferencing performance of GEOEYE-1. *Photogramm. Eng. Rem. Sens.* 75 (6), 634–638.
- Furukawa, Y., Ponce, J., 2010. Accurate, dense, and robust multiview stereopsis. *IEEE Trans. Pattern Anal. Mach. Intell.* 32 (8), 1362–1376.
- Fusiello, A., Trucco, E., Verri, A., 2000. A compact algorithm for rectification of stereo pairs. *Mach. Vis. Appl.* 12 (1), 16–22.
- Garvin, J.B., Sakimoto, S., Schnetzer, C., Frawley, J.J., 1999. Global Geometric Properties of Martian Impact Craters: a Preliminary Assessment Using Mars Orbiter Laser Altimeter (MOLA).
- Grodecki, J., Dial, G., 2003. Block adjustment of high-resolution satellite images described by rational polynomials. *Photogramm. Eng. Rem. Sens.* 69 (1), 59–68.
- Hastie, T., Tibshirani, R., Friedman, J., 2009. The Elements of Statistical Learning, second ed. Springer, Berlin, Germany, p. 763.
- Henriksen, M.R., Manheim, M.R., Burns, K.N., Seymour, P., Speyerer, E.J., Deran, A., Boyd, A.K., Howington-Kraus, E., Rosiek, M.R., Archinal, B.A., 2017. Extracting accurate and precise topography from LROC narrow angle camera stereo observations. *Icarus* 283, 122–137.
- Hirschmüller, H., 2008. Stereo processing by semiglobal matching and mutual information. *IEEE Trans. Pattern Anal. Mach. Intell.* 30 (2), 328–341.
- Hu, H., Chen, C., Wu, B., Yang, X., Zhu, Q., Ding, Y., 2016a. Texture-aware Dense Image Matching Using Ternary Census Transform. *ISPRS Annals of the Photogrammetry, Remote Sensing and Spatial Information Sciences III-3*, pp. 59–66.
- Hu, H., Ding, Y., Zhu, Q., Wu, B., Xie, L., Chen, M., 2016b. Stable least-squares matching for oblique images using bound constrained optimization and a robust loss function. *ISPRS J. Photogrammetry Remote Sens.* 118, 53–67.
- Kim, T., 2000. A study on the epipolarity of linear pushbroom images. *Photogramm. Eng. Rem. Sens.* 66 (8), 961–966.
- Kolmogorov, V., Zabih, R., 2001. Computing visual correspondence with occlusions using graph cuts. In: Proc. 9th IEEE International Conference on Computer Vision (ICCV2001). IEEE, Vancouver, British Columbia, Canada, pp. 508–515. July 7–14.
- Li, R., Hwangbo, J., Chen, Y., Di, K., 2011. Rigorous photogrammetric processing of HiRISE stereo imagery for Mars topographic mapping. *IEEE Trans. Geosci. Rem. Sens.* 49 (7), 2558–2572.
- Loop, C., Zhengyou, Z., 1999. Computing rectifying homographies for stereo vision. In: Proc. Computer Vision and Pattern Recognition, 1999. IEEE Computer Society Conference on, vol. 1, p. 131.
- Matsson, S., Ojha, L., Ortiz, A., McEwen, A.S., Burns, K., 2012. Regional digital terrain model production with LROC-NAC. In: Proc. Lunar and Planetary Science Conference, the Woodlands, Texas, USA, March 19–23.
- Moisan, L., Mouloua, P., Monasse, P., 2012. Automatic homographic registration of a pair of images, with a contrario elimination of outliers. *Image Process. Line* 2, 56–73.
- Moratto, Z.M., McMichael, S.T., Beyer, R.A., Alexandrov, O., Fong, T., 2014. Automated and accurate: making DTMs from LRO-NAC using the ames stereo pipeline. In: Proc. Lunar and Planetary Science Conference, the Woodlands, Texas, USA, March 17–21, p. 2892.

- Oh, J., Lee, W.H., Toth, C.K., Grejner-Brzezinska, D.A., Lee, C., 2010. A piecewise approach to epipolar resampling of pushbroom satellite images based on RPC. *Photogramm. Eng. Rem. Sens.* 76 (12), 1353–1363.
- Robinson, M.S., Brylow, S.M., Tschimmel, M., Humm, D., Lawrence, S.J., Thomas, P.C., Denevi, B.W., Bowman-Cisneros, E., Zerr, J., Ravine, M.A., 2010. Lunar reconnaissance orbiter camera (LROC) instrument overview. *Space Sci. Rev.* 150 (1), 81–124.
- Scharstein, D., Szeliski, R., 2002. A taxonomy and evaluation of dense two-frame stereo correspondence algorithms. *Int. J. Comput. Vis.* 47 (1), 7–42.
- Scharstein, D., Szeliski, R., Hirschmüller, H., 2017. Middlebury Stereo Evaluation - Version 3. <http://vision.middlebury.edu/stereo/eval3/> (Accessed 19th December, 2017).
- Smith, D.E., Zuber, M.T., Frey, H.V., Garvin, J.B., Head, J.W., Muhleman, D.O., Pettengill, G.H., Phillips, R.J., Solomon, S.C., Zwally, H.J., 2001. Mars orbiter laser altimeter: experiment summary after the first year of global mapping of Mars. *J. Geophys. Res.: Plan.* 106 (E10), 23689–23722.
- Smith, D.E., Zuber, M.T., Jackson, G.B., Cavanaugh, J.F., Neumann, G.A., Riris, H., Sun, X., Zellar, R.S., Coltharp, C., Connelly, J., Katz, R.B., Kleyner, I., Liiva, P., Matuszeski, A., Mazarico, E.M., McGarry, J.F., Novo-Gradac, A., Ott, M.N., Peters, C., Ramos-Izquierdo, L.A., Ramsey, L., Rowlands, D.D., Schmidt, S., Scott, V.S., Shaw, G.B., Smith, J.C., Swinski, J., Torrence, M.H., Unger, G., Yu, A.W., Zagwodzki, T.W., 2010. The lunar orbiter laser altimeter investigation on the lunar reconnaissance orbiter mission. *Space Science Reviews* 150 (1–4), 209–241.
- Speyerer, E.J., Wagner, R.V., Robinson, M.S., Licht, A., Thomas, P.C., Becker, K., Anderson, J., Brylow, S.M., Humm, D.C., Tschimmel, M., 2016. Pre-flight and on-orbit geometric calibration of the lunar reconnaissance orbiter camera. *Space Sci. Rev.* 200 (1–4), 357–392.
- Tran, T., Rosiek, M.R., Howington-Kraus, E., Archinal, B.A., Anderson, E., Team, L.S., 2010. Generating digital terrain models using LROC NAC images. In: Proc, pp. 15–19.
- USGS, 2017. Integrated Software for Imagers and Spectrometers. <https://isis.astrogeology.usgs.gov/> (Accessed 3rd June, 2017).
- Wang, M., Hu, F., Li, J., 2011. Epipolar resampling of linear pushbroom satellite imagery by a new epipolarity model. *ISPRS J. Photogrammetry Remote Sens.* 66 (3), 347–355.
- Watters, W.A., Geiger, L.M., Fendrock, M., Gibson, R., 2015. Morphometry of small recent impact craters on Mars: size and terrain dependence, short-term modification. *J. Geophys. Res.: Plan.* 120 (2), 226–254.
- Wu, B., Hu, H., Guo, J., 2014. Integration of Chang'E-2 imagery and LRO laser altimeter data with a combined block adjustment for precision lunar topographic modeling. *Earth Planet. Sci. Lett.* 391, 1–15.
- Wu, B., Liu, W.C., 2017. Calibration of boresight offset of LROC NAC imagery for precision lunar topographic mapping. *ISPRS J. Photogrammetry Remote Sens.* 128, 372–387.
- Wu, B., Zhang, Y., Zhu, Q., 2012. Integrated point and edge matching on poor textural images constrained by self-adaptive triangulations. *ISPRS J. Photogrammetry Remote Sens.* 68, 40–55.
- Wu, B., Guo, J., Hu, H., Li, Z., Chen, Y., 2013. Co-registration of lunar topographic models derived from Chang'E-1, SELENE, and LRO laser altimeter data based on a novel surface matching method. *Earth and Planetary Science Letters* 364, 68–84.